ACS OMEGA

http://pubs.acs.org/journal/acsodf
Article

Crystallization Retardation and Synergistic Trap Passivation in Perovskite Solar Cells Incorporated with Magnesium-Decorated Graphene Quantum Dots

Somayeh Kalanaki, Yaser Abdi, and Fatemeh Rahnemaye Rahsepar*

Cite This: ACS Omega 2023, 8, 38345−38358
Read Online

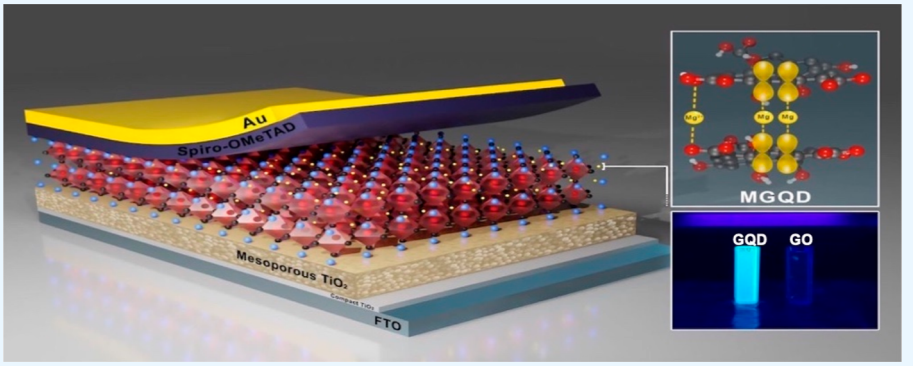

ABSTRACT: One of the encouraging strategies for enhancing the efficiency of perovskite solar cells (PSCs) is to reduce defects, trap states of pinholes, and charge recombination rate in the light absorber layer of perovskite, which can be addressed by increasing the perovskite grain size. The utilization of Mg-decorated graphene quantum dots (MGQD) or graphene quantum dots (GQDs) into a perovskite precursor solution for further crystal modification is introduced in this study. Studies on the crystalline structure and morphology of MGQD generated from GQDs demonstrate that MGQD has a greater crystal size than GQD. Therefore, higher light absorption in the whole UV−vis spectrum and a larger grain size for the perovskite/MGQD layer compared to the perovskite/GQD sample are achieved. Moreover, more photoluminescence peak quenching of perovskite/MGQD and extended carrier recombination lifetime (from 3 to 40 ns) verify the surface and grain boundary trap passivation compared to pristine perovskite. Consequently, PSCs in an n-i-p configuration containing perovskite/MGQD show a higher performance of 10.2% in comparison to the pristine perovskite at 7.2%, attributed to the enhanced J_{SC} from 13.2 to 19.1 mA cm^{-2}. Thus, incorporating MGQDs into the perovskite layer is a hopeful approach for obtaining a superior perovskite film with impressive charge extraction and decreased nonradiative charge recombination.

1. INTRODUCTION

The functionalization and decoration of graphene quantum dots (GQDs) are under intensive investigation because of their potential applications in the research community for the optoelectronic arena. In general, two main procedures are utilized for the synthesis of GQDs: the bottom-up[1] and the top-down methods.[2] The ultrasonic method, as a subcategory of the top-down technique, is mostly conducted for GQD synthesis thanks to its low cost, large-scale preparation, and facile manipulation.[3,4] In this technique, as a result of the instantaneous high pressure and energy of ultrasonic waves, countless small bubbles are produced in liquid, which forces graphite layers to shrink, collapse, and destroy carbon−carbon bonds.[5] The GQDs are large-band gap semiconductors with specific properties such as size-dependent band gap tailoring, stable photoluminescence (PL), and edge effects, in addition to special quantum confinement. In light of the significant properties of GQDs, they are widely known as potential candidates for optoelectronic applications such as photodetection over a broad wavelength range,[6] photovoltaic (PV) devices,[7] and light-emitting diodes.[8]

Photovoltaic devices have been developed as a renewable, clean energy technology to tackle serious global warming environmental issues.[9] Perovskite solar cells (PSCs) are the most encouraging emerging PV technology because of their low cost,[10,11] simple solution processing,[12] high optical absorption coefficients over the solar spectrum, tunable

Received: July 3, 2023
Accepted: September 19, 2023
Published: October 2, 2023

https://doi.org/10.1021/acsomega.3c04734
ACS Omega 2023, 8, 38345−38358

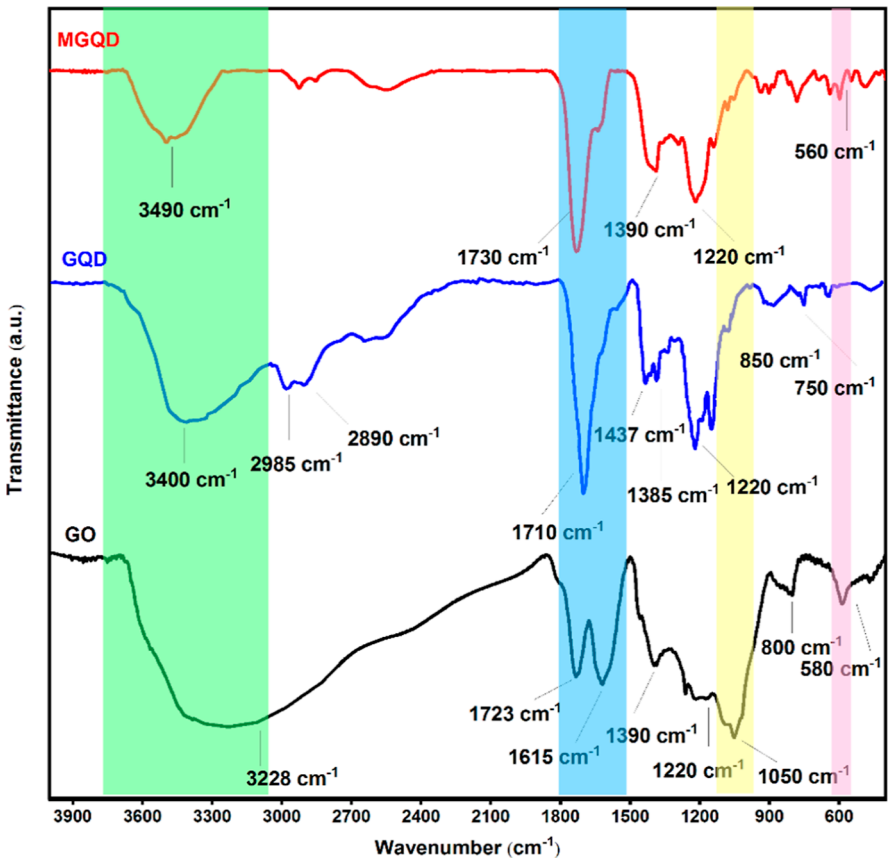

Figure 1. FTIR spectra of GO, GQD, and MGQD. The green (3750−3100 cm^{-1}), blue (1800−1530 cm^{-1}), yellow (1250−1050 cm^{-1}), and pink (610−580 cm^{-1}) highlighted regions correspond to stretching vibration of hydroxyl, carbonyl, aromatic C═C, C−O−C and bending vibration of C−O−C groups, respectively.

bandgap,[13] low exciton binding energies,[14] long-range carrier diffusion,[15] and high defect tolerance.[16] Organic−inorganic hybrid PSCs have made rapid progress, where the power conversion efficiency (PCE) has advanced drastically from 3.8[17] to 25.7%[18,19] in the past decade. This type of semiconductor has an ABX_3 structure, where A is methylammonium (MA), formamidinium, or cesium (Cs); B is Pb or Sn; and X can be replaced by I, Br, or Cl.[20] Several approaches, such as compositional and interfacial engineering,[21−23] have been investigated to boost the performance of PSCs.[24,25] One of the most critical factors in enhancing the PCE of PSCs is controlling the perovskite layer morphology to deposit a pinhole-free, highly crystalline, and homogeneous larger grain-size film.[26−28] Since the perovskite layer grain boundaries are considered as the charge trapping sites and recombination centers, grain boundaries are reduced by having a larger perovskite grain diameter which enhances the charge carrier mobility and collection efficiency simultaneously.[29] To date, various approaches, including changes in the annealing condition,[30] solvent engineering during the fabrication process,[31] and incorporation of additives such as carbon-based nanostructures,[32−36] chloride salt,[18,37,38] and polyvinylpyrrolidone,[22,39] have been applied for adjusting the crystalline structure and surface morphology[40] of the perovskite layer, which translates to higher performance. Therefore, the effective incorporation of carbon-based derivatives into the perovskite solution is regarded as a promising and outstanding approach toward further improvement of the perovskite film quality.

The application of graphene and GQDs has been previously studied in PSCs.[41] The enhancement in PV performance has been observed from 18.6 to 20.5% by applying tiny GQDs < 5 nm particles between the mesoporous TiO_2 layer and perovskite film,[42] which is attributed to distinct electron extraction channels in the presence of GQDs. Graphene and GQD, additionally, have been integrated into the perovskite layer as a technique to change the perovskite grain boundaries, resulting not only in an enhancement in the crystal size of the perovskite film but also in the promotion of electron transport in the layer of perovskite.[35,36] Furthermore, the incorporation of GQD in the perovskite layer brought about an 11% improvement in PCE of PSCs due to better crystallization of the perovskite film with lower defects in grain boundaries and interfaces, resulting in better charge collection, descent charge extraction, and thus lower nonradiative charge recombination. Since the chemical composition of the perovskite layer determines their electrical and optical properties, doping other metallic cations instead of lead can effectively modify perovskite trap passivation and crystal modification, and the use of appropriate electron and hole extraction layers can assist the performance and stability of the Pb-free PSCs.[43] In addition, ion doping is also employed as another impressive approach to controlling carrier transport and trap density.[44] Using alkali metal salts such as KI additive in the perovskite precursor solution, the perovskite film grain size was reported to increase substantially even at a low doping level, resulting in an improvement of PCE from 13.8 to 15.3%.[44]

https://doi.org/10.1021/acsomega.3c04734
ACS Omega 2023, 8, 38345−38358

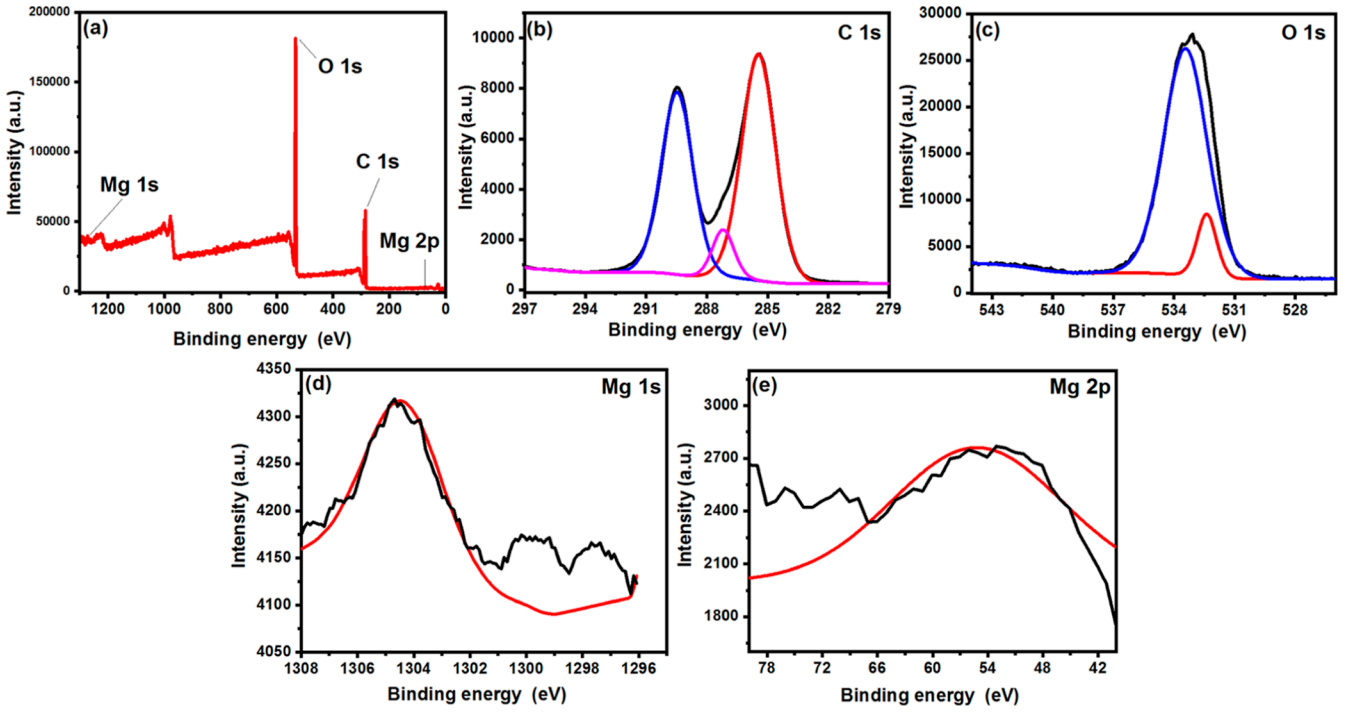

Figure 2. XPS spectra of (a) survey, (b) C 1s, (c) O 1s, (d) Mg 1s, and (e) Mg 2p regions of MGQD.

Despite the great efforts to study the effect of doping metal cations in PSCs, studies on magnesium (Mg) as an effective dopant have not received much attention except for its incorporation into the dense TiO_2 electron transport layer (ETL) of planar PSCs.[45,46] These reports have shown that Mg doping is capable of transferring the Fermi energy level of the ETL atop, reducing the buried trap states, and increasing the free electron density, where more than 19% PCE has been obtained through the incorporation of Mg into the TiO_2 layer of PSCs.[47] In addition, previous reports on interface engineering by incorporating N, S-codoped GQDs (NSGQDs)[33] or nitrogen-doped GQDs (N-GQDs)[48,49] in the ETL/perovskite interlayer or utilizing the N-GQDs energy-down-shift layer on top of the fully inorganic PSCs[50] as well as using functional semiconductor additives in perovskite films such as graphite-nitrogen-doped GQDs,[51] revealed the beneficial properties of doped-GQD in PV performance of PSCs. As far as we know, no research has been conducted on the systematic incorporation of Mg^{2+}-doped GQDs into the perovskite layer and its influence on the PV parameters of PSCs. The concept of using Mg^{2+} ions is that magnesium in the porphyrin ring of chlorophyll found in plant green leaves is the main stabilizer of the molecule, which absorbs sunlight and converts it into energy by transferring electrons.[52]

In this study, GQDs were synthesized from graphene oxide (GO) through an economical ultrasonic method and then decorated with Mg^{2+} to obtain Mg-doped GQDs (MGQDs). Thus, Mg^{2+} and GQD were simultaneously incorporated into the perovskite layer to render trap states and boost PV performance. To that purpose, the synthesized MGQD was added directly to the precursor solution of perovskite as an additive. The impact of its incorporation on the structure, morphology, and optical properties of the perovskite absorber layer, as well as the electro-optical properties of PSCs with a conventional configuration of fluorine-doped tin oxide (FTO)/compact TiO_2/meso-porous TiO_2/perovskite/spiro-OMeTAD/Au, was investigated.

2. RESULTS AND DISCUSSION

2.1. Characterization of GO, GQD, and MGQD Samples. Considering the synthesis methods, sonication of GO caused cleavage of C═C and C−O−C bonds, increasing the number of sp^3 carbons and further oxidizing the GO. Furthermore, due to the well-known capability of Mg^{2+} to bind to oxygen-containing functional groups,[53] it is expected that Mg^{2+} can be readily decorated into GQD via the formation of a network with hydroxyl and carboxyl groups of GQD. In other words, Mg^{2+} ions serve as a cross-linking agent between adjacent GQDs.

To pursue the variations in chemical composition during the synthesis of MGQD from GO, Fourier transform infrared (FTIR) spectroscopy was conducted. Figure 1 depicts the FTIR spectra of GO, GQD, and MGQD samples with four highlighted regions attributed to the stretching vibration of hydroxyl, carbonyl, and aromatic C═C, C−O−C, and the bending vibration of C−O−C groups. The characteristic peaks of GO as a compound with abundant oxygen-containing groups appeared at 1220, 1390, 1620, and 1720 and a broad peak at 3300 cm^{-1}, which are related to stretching vibration of alkoxy C−O, carboxy C−O, C═C, C═O, and O−H groups, respectively.[53] The existence of bands located at 1052 and 580 cm^{-1} corresponds to the stretching and bending vibration of epoxy C−O−C, respectively.[54] Furthermore, the peak at 800 cm^{-1} is attributed to the C−H (aromatic ring) stretching vibration. After sonication of GO to obtain GQD, new peaks at 750, 2890, and 2985 cm^{-1} assigned to CH_2 rocking and asymmetrical and symmetrical stretching vibrations of C−H appeared, respectively, while the C═C peak at 1615 cm^{-1} decreased dramatically where the peaks assigned to epoxy C−O−C disappeared.[55,56] These results confirm the breakage of C═C and the opening of the epoxide ring during GQD

https://doi.org/10.1021/acsomega.3c04734
ACS Omega 2023, 8, 38345−38358

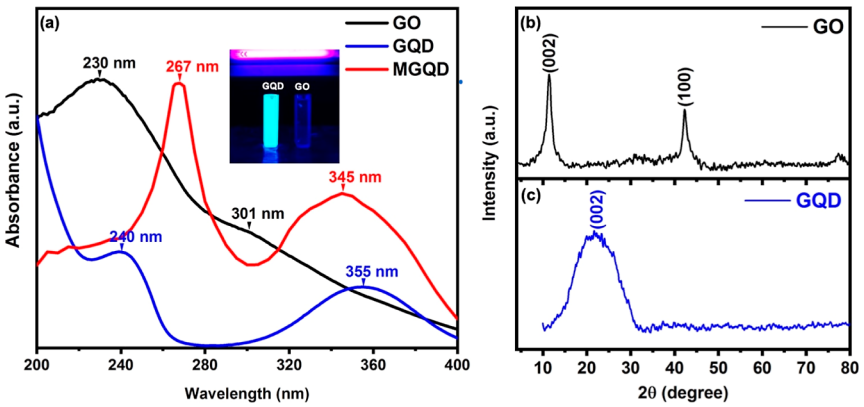

Figure 3. (a) UV−vis spectra of GO, GQD, and MGQD samples (inset: the PL of GQD under the UV light, while GO did not show any PL). The XRD patterns of (b) GO and (c) GQD samples.

synthesis. In addition, the peak found at 1437 and 850 cm^{-1} was regarded as in-plane and out-of-plane bending vibrations of O−H, respectively, produced by the breakage of the C−O−C group.[53] After decorating the GQD support with $MgCl_2$, due to the direct coordination of Mg^{2+} with oxygen-containing groups, the peaks related to C═O (1730 cm^{-1}) and OH (3300 cm^{-1}) shifted to a higher wavenumber with increased intensity. The increased FTIR intensities caused by the incorporation of $MgCl_2$ in GO due to the complexation of Mg^{2+} ions with carboxylic groups were confirmed in previous reports.[53] Moreover, the weak peak at 560 cm^{-1} could be dedicated to the Mg−O stretching vibration, indicating the presence of Mg in the GQD structure (MGQD sample).

Additional support for the introduction of Mg into the chemical structure of the GQD derives from X-ray photoelectron spectroscopy (XPS). High-resolution XPS spectra of the C 1s, O 1s, Mg 1s, and Mg 2p regions are displayed in Figure 2. According to the survey spectrum (Figure 2a), there are two peaks with high intensity at 285 and 533 eV related to C 1s and O 1s, respectively. The higher intensity of the oxygen peak in comparison to carbon indicated the existence of a larger amount of oxygen-rich functional groups in the chemical structure of MGQD that can boost the possibility of their coordination with Mg^{2+}. The high-resolution XPS spectrum of C 1s (see Figure 2b) implied three fitted peaks at 285.45, 287.19, and 289.45 eV, which can be assigned to the alkyl carbon atom in $C(sp^3)$/C−OH, the carbonyl C in the C═O and the carbonyl C in the COOH functional groups of the MGQD structure, respectively. As shown in Figure 2b, there was a significant change in the surface chemistry of GQD due to the incorporation of Mg. The C 1s component corresponding to C═C was not seen in the XPS spectrum of C 1s. The reason could be due to the coverage of the GQD surface by Mg^{2+} ions and the strong cation−π interactions between Mg^{2+} and a few C═C bonds present on the surface of GQD.

Meanwhile, the corresponding O 1s spectrum of MGQD (see Figure 2c) showed two peaks appearing at 532.38 and 533.43 eV, assigning to C═O in carboxylic acid and C−OH bonds, respectively.[57,58] The results confirmed that the prepared GQD was rich in carboxylic acid and hydroxyl groups, making it ready to interact with Mg^{2+}. Besides C 1s and O 1s, there were two low-intensity peaks at 50.1 and 1305.08 eV, corresponding to Mg 1s and Mg 2p in Figure 2d,e, respectively, which indicate the decorating of Mg^{2+} into GQD structure through interaction with oxygen-containing groups or π electrons of C═C bonds.[53] However, the absence of any Cl 2p feature at about 200 eV affirmed the removal of Cl^- from the surface of the MGQD during the washing process.

Furthermore, to investigate the optical properties of GO, GQD, and the effect of Mg-decorating on GQD properties, UV−vis spectroscopy was conducted. As can be seen in Figure 3a, GO exhibits a prominent peak at 230 nm and a low-intensity peak at 301 nm, assigned to the $\pi \rightarrow \pi^*$ transition of conjugate double bonds of aromatic groups and the $n \rightarrow \pi^*$ transition of heteroatoms in oxygen-containing functional groups present in GO, respectively.[59] The optical properties of the GQDs are strongly influenced by edge effects generated by size reduction.[60] As presented in the inset of Figure 3a, the GQD apparently showed PL under UV light, whereas the GO one did not have any PL. It can be attributed to GO cutting into small pieces by ultrasonication, which results in an increment in the number of edges and the attaching oxygen-containing groups in GQD. Compared to the GO sample, there is a significant decrease in intensity of the peak corresponding to the $\pi \rightarrow \pi^*$ transition along with a slight red shift to 240 nm in the GQD UV−vis spectrum, which implied the breakage of conjugate double bonds and an increase in electron-withdrawing groups such as carbonyl and carboxylic acid near C═C bonds. Moreover, the increase in oxygen-rich group content at the edge of GQD caused intensity enhancement and red shift of the $n \rightarrow \pi^*$ transition peak to 355 nm. By introducing Mg^{2+} to GQD, the peak linked to $\pi \rightarrow \pi^*$ transition shifted to a higher wavelength (267 nm, compared to GQD). This red shift is because of the strong π-cation interaction between Mg^{2+} and π electrons of C═C. Moreover, the $n \rightarrow \pi^*$ transition blue-shifted to 345 nm compared to GQD due to effective dipole interaction between Mg^{2+} and lone pairs of electrons in oxygen atoms of carboxyl or hydroxyl groups, which resulted in a diminished energy level of the nonbonding state and increased the band gap (Figure 3a).

The effect of Mg-decorating on the crystallinity of the GQD was investigated by operating XRD measurements. The XRD patterns of GO and GQD samples are demonstrated in Figure 3b,c. In the case of GO (see Figure 3b), the diffraction peak at 2θ = 11.3° was related to the (002) plane with a d-spacing of 0.78 nm. The relatively strong peak at 2θ = 42.3° was attributed to the (100) plane, which was assigned to the amorphous state of GO, as reported previously.[61] The appearance of the (002) diffraction peak at 2θ = 22.45° (d-spacing of 0.39 nm) in the XRD spectrum of GQD (see Figure

https://doi.org/10.1021/acsomega.3c04734
ACS Omega 2023, 8, 38345−38358

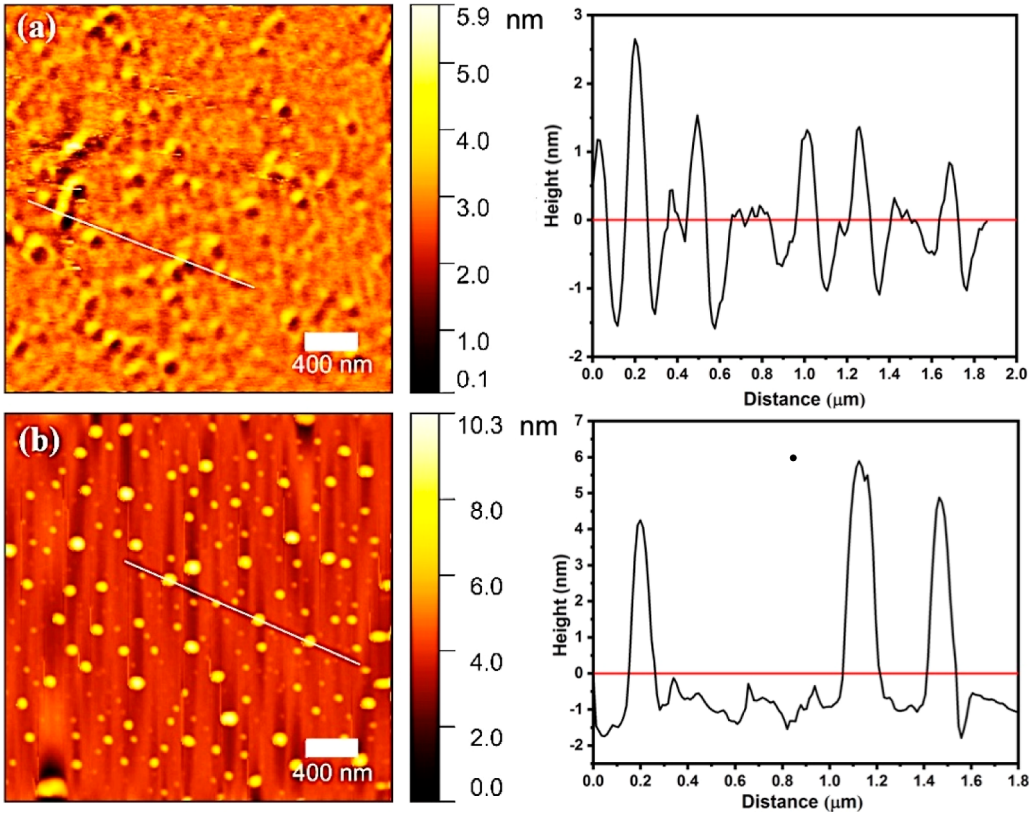

Figure 4. AFM images and height profiles of (a) GQD and (b) MGQD.

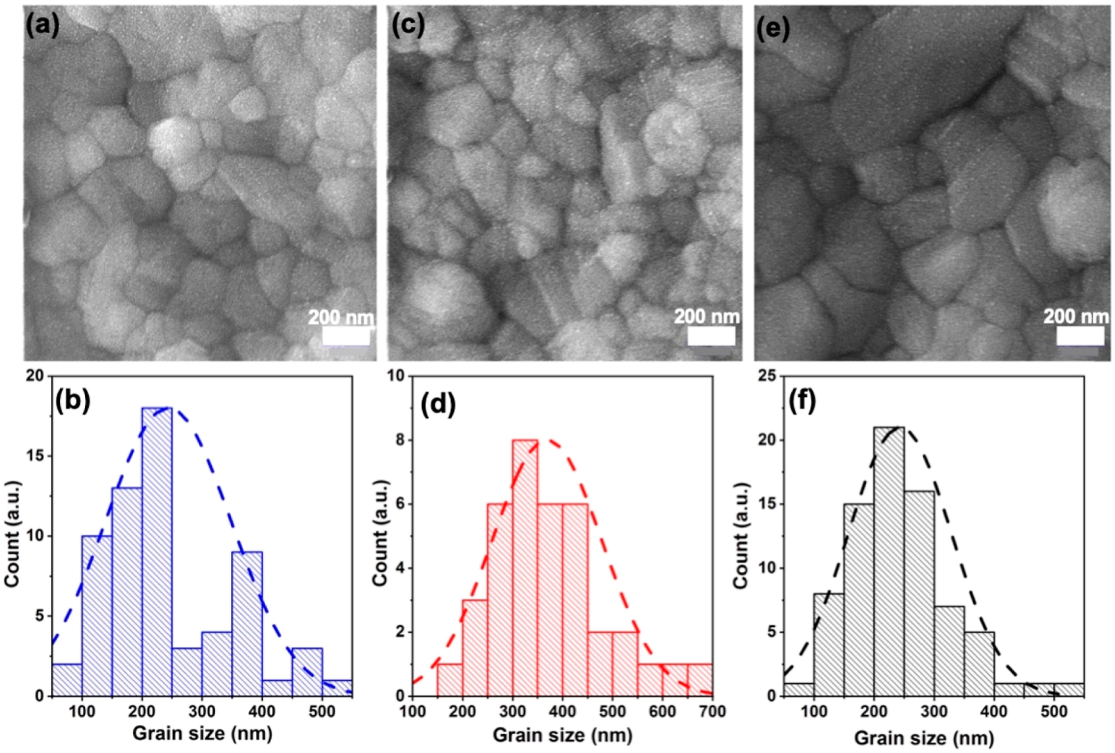

Figure 5. Top view FE-SEM images and the corresponding size distribution histogram of (a,b) pristine perovskite, (c,d) perovskite/GQD, and (e,f) perovskite/MGQD samples deposited on a glass substrate. The scale bars of the FE-SEM images correspond to 200 nm.

3c) presented the restoration of a destroyed network of carbon atoms after sonication. Moreover, the (002) diffraction peak was broader than GO, indicating a broad distribution of the GQD size with only a few graphene sheets.[60,62] The GQD crystallite size was calculated to be 0.68 nm by the Debye–Scherrer equation.[63]

https://doi.org/10.1021/acsomega.3c04734
ACS Omega 2023, 8, 38345−38358

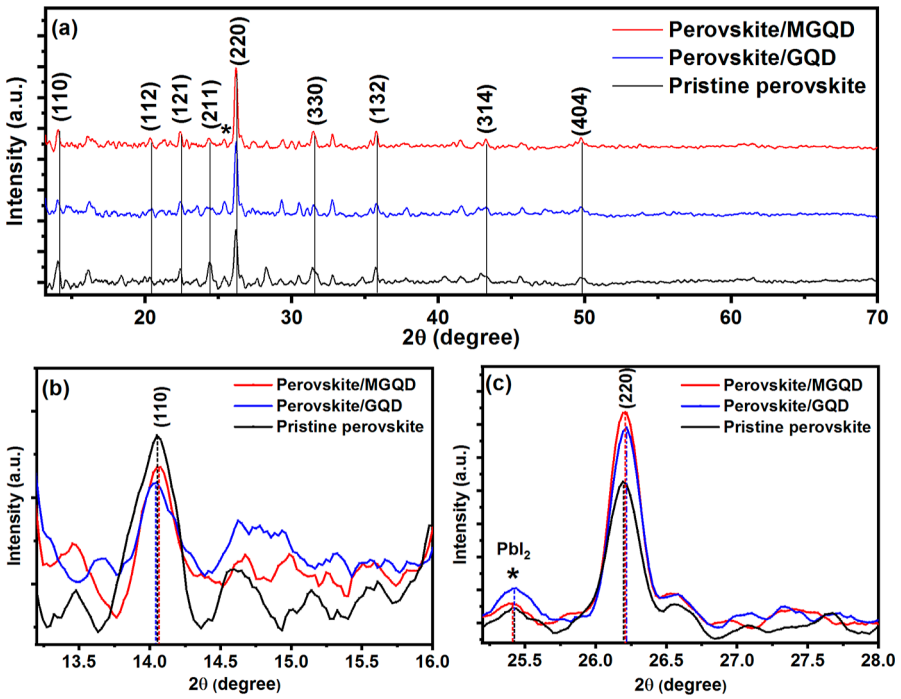

Figure 6. XRD spectra of (a) pristine perovskite (black), perovskite/GQD (blue), and perovskite/MGQD (red) samples and (b,c) magnified XRD pattern of the corresponding samples.

Furthermore, the TEM images of GQD and MGQD samples, along with the corresponding histogram nanoparticle size distribution, are displayed in Figure S1a–d. As shown in Figure S1a,b, the as-prepared GQD are almost spherical, with an average size between 10 and 20 nm, confirming the quantum nature of the synthesized GQD.[36] The presence of particles greater than 20 nm was due to the stacking of tiny particles of GQD.[64] By incorporating $MgCl_2$ in GQD, the crystal structure of GQD altered and the average particle size increased to about 50 nm, indicating successful intercalation of Mg^{2+} ions into GQD (see Figure S1c,d).

The AFM measurements were conducted to get much deeper investigations on the surface topographic height of the GQD upon decorating with $MgCl_2$. Figure 4a,b show the AFM images of GQD and MGQD with their corresponding height profiles, respectively. The observed topographic height of the GQD sample (see Figure 4a) was about 2 nm, confirming the presence of 2–6 layers of graphene in each individual GQD, proofing the high quality of the synthesized GQD.[65,66] For the MGQD sample, the topographic height is increased to 5–6 nm upon modification of the GQD with $MgCl_2$ (see Figure 4b). The observed increase in the height of particles is alternative proof for the hypothesis that Mg^{2+} ions act as a cross-linking agent between adjacent GQDs.

2.2. Characterization of GQD- and MGQD-Doped Perovskite Films. To consider the effect of GQD and MGQDs on the perovskite layers and the performance of photovoltaic devices, GQD and MGQDs powders were added to the precursor solution of perovskite (see Experimental Section) and labeled as perovskite/GQD and perovskite/MGQD. To inspect the role of GQD and MGQD on crystallinity and grain size of perovskite film, pristine perovskite, and modified perovskite ink were deposited on the FTO/compact TiO_2/Meso-porous TiO_2 substrate, and their morphology and crystal structure were characterized using field-emission scanning electron microscopy (FE-SEM) images and XRD analysis, respectively.

Figure 5a–f shows the top surface FE-SEM images of pristine perovskite, perovskite/GQD, and perovskite/MGQD films and the corresponding grain size distribution histogram. As it is evident from Figure 5a, the pristine perovskite film had a uniform and smooth morphology with several pinhole defects, and based on the size distribution histogram (Figure 5b), the perovskite crystal size ranged from 100 to 400 nm with an average grain size of 250 nm. The presence of tiny crystals caused an enlargement in the grain boundaries, and therefore, the number of pinhole defects that act as charge recombination sites increased.[35] Since the pinhole defects can be effectively eliminated by increasing the grain size, by adding GQD to the perovskite precursor solution, the number of crystals larger than 300 nm increased significantly, while there was no change in the average grain size (see Figure 5c,d). The introduction of GQDs had two separate effects on the crystallization of perovskite grains: (i) GQDs retarded the crystallization process and caused a decrease in the number of nucleates and hence better perovskite crystals with a larger size, and (ii) the polar functional groups on GQD, including hydroxyl, carbonyl, and carboxylic acid, interact strongly with the perovskite precursors, making effective contact with the grains of the perovskite layer and hence, better crystallization.[35,36] According to Figure 5e,f, upon dispersion of MGQD into perovskite precursor solution, the grain average size of the perovskite increased to about 350 nm, as well as boosting the number of crystals larger than 300 nm, which means a few grain boundaries. In addition, the continuous and narrow distribution histograms presented in Figure 5d,f (compared to the histogram of Figure 5b, which has a nonuniform distribution at sizes ~250–300 nm) resulted from the retarded rapid nucleation kinetics and formation of uniform and oriented crystals. Moreover, the presence of Mg^{2+} ions made the interaction of perovskite with MGQD stronger, which

https://doi.org/10.1021/acsomega.3c04734
ACS Omega 2023, 8, 38345–38358

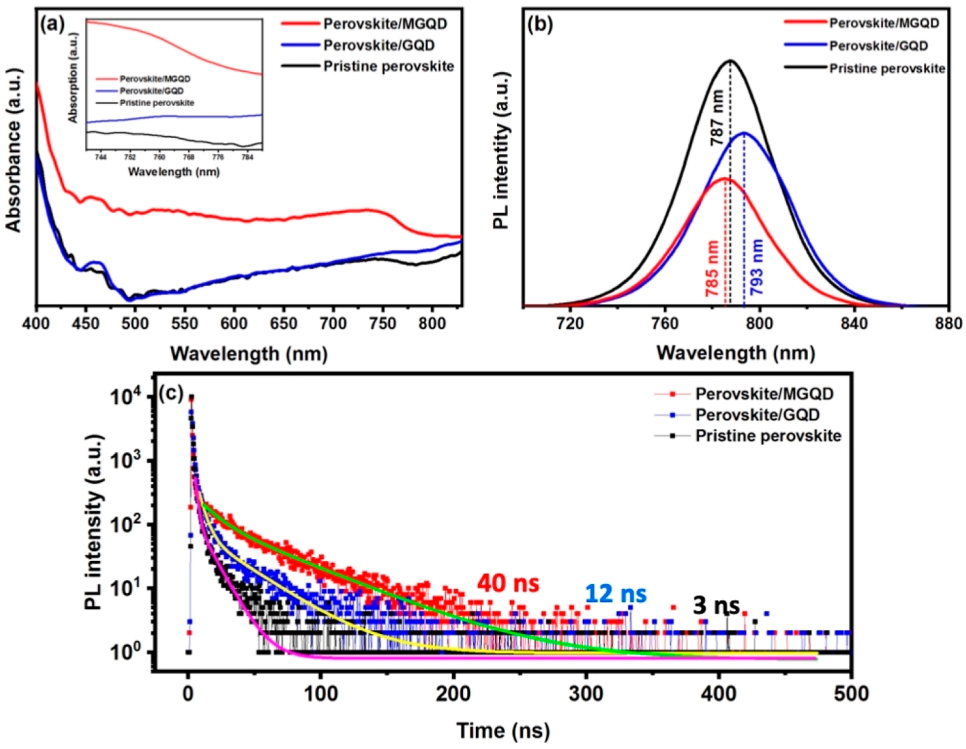

Figure 7. (a) UV−vis absorption and (b) steady state and (c) time-resolved PL spectra of glass/pristine perovskite, glass/perovskite/GQD, and glass/perovskite/MGQD samples; included are the extracted average lifetimes fitted with a double-exponential decay function.

retarded the crystallization process, and larger perovskite grains were achieved. It is also noteworthy that due to the modification in the grain size of perovskite/GQD and perovskite/MGQD samples compared to pristine perovskite layers, the trap states and pinhole defects of grain boundaries in the treated layers have been suppressed, which could lead to more efficient charge transport.[67]

To evaluate the effect of GQD and MGQD incorporation on the crystalline structure of the perovskite layer, XRD analysis was carried out on pristine perovskite, perovskite/GQD, and perovskite/MGQD samples, as shown in Figure 6a−c. The XRD patterns show that there was almost no difference in the peak positions of perovskite layers with and without GQD and MGQD. The diffraction peaks at 14.07, 20.18, 22.4, 24.45, 26.23, 31.6, 35.8, 43.12, and 49.8° are indexed to (110), (112), (121), (211), (220), (330), (132), (314), and (404) planes, which are characteristic of the tetragonal phase of $MAPbI_3$.[36,68] Regarding the XRD of perovskite/GQD and perovskite/MGQD samples, the patterns show no diffraction peaks corresponding to GQD and MGQD owing to the small decoration. Moreover, the fwhm of the XRD pattern, especially the one centered at 26.23°, decreased in the order of pristine perovskite > perovskite/GQD > perovskite/MGQD, and based on the Scherrer equation, these changes demonstrated the modification in grain size and crystalline structure of perovskite film when it was incorporated with GQD and MGQD (Figure 6c).[33,35] These outcomes aligned well with the FE-SEM images (Figure 5a−f). Moreover, the detrimental PbI_2 peak at 25.2° and the main peak of (110) at 14.07° were reduced in the case of perovskite/MGQD compared to the perovskite/GQD pattern (Figure 6b,c).

Moreover, the effects of GQD and MGQD on the absorption and PL properties of the perovskite layer were investigated, which are shown in Figure 7a,b, respectively. In comparison with the pristine perovskite, the perovskite/MGQD sample demonstrated enhanced absorption, while the perovskite/GQD sample's absorption intensity did not significantly change (Figure 7a). This may be attributed to the passivation effect and fluorescence quantum effect of GQDs, which can restrict trapping the photogenerated electrons at grain boundaries.[36] On the other hand, according to the FE-SEM images of the perovskite/MGQD sample (Figure 5e), with a substantial enhancement in the grain size of perovskite/MGQD compared to pristine perovskite (Figure 5b) and therefore higher crystallinity in each grain, the absorption intensities of perovskite/MGQD increased.[67,69] The FE-SEM image of the perovskite/GQD (Figure 5d) sample revealed that the size of the crystals did not change significantly compared to that of the untreated perovskite films (Figure 5b), resulting in a small difference in the absorption spectra between perovskite/GQD and pristine perovskite (Figure 7a).

The PL spectra of perovskite/MGQD, perovskite/GQD, and pristine perovskite samples on the FTO/compact TiO_2/Meso-porous TiO_2 substrate were measured (Figure 7b) to evaluate the effect of the introduction of GQD or MGQD on charge extraction and recombination rate. All samples exhibited a PL peak at around 785 nm, ascending from the perovskite conduction to the valence band radiative charge recombination.[70] The PL peak intensities of perovskite/MGQD and perovskite/GQD were largely reduced compared to those of pristine perovskite. Such dramatic PL quenching was due to reinforcing charge carrier extraction from the modified perovskite layer with GQDs or MGQD to underneath ETL.[36] The most quenching was obtained for perovskite/MGQD, which can be attributed to the synergistic passivation of surface trap states, reduced nonradiative recombination, improvement in morphology, and formation of semiconductor−semiconductor interfaces.[26] Moreover, the

https://doi.org/10.1021/acsomega.3c04734
ACS Omega 2023, 8, 38345−38358

Table 1. Summary of the Carrier Lifetime Estimated from Fitting the TRPL Spectra Reported in Figure 7C

samples	τ_1 (ns)	A_1 (%)	τ_2 (ns)	A_2 (%)	$\tau_{avg} = \frac{A_1\tau_1^2 + A_2\tau_2^2}{A_1\tau_1 + A_2\tau_2}$ (ns)
pristine perovskite	1.87	0.98	11.18	0.02	3
perovskite/GQD	4.66	0.94	31.18	0.06	12
perovskite/MGQD	13.39	0.63	52.03	0.37	40

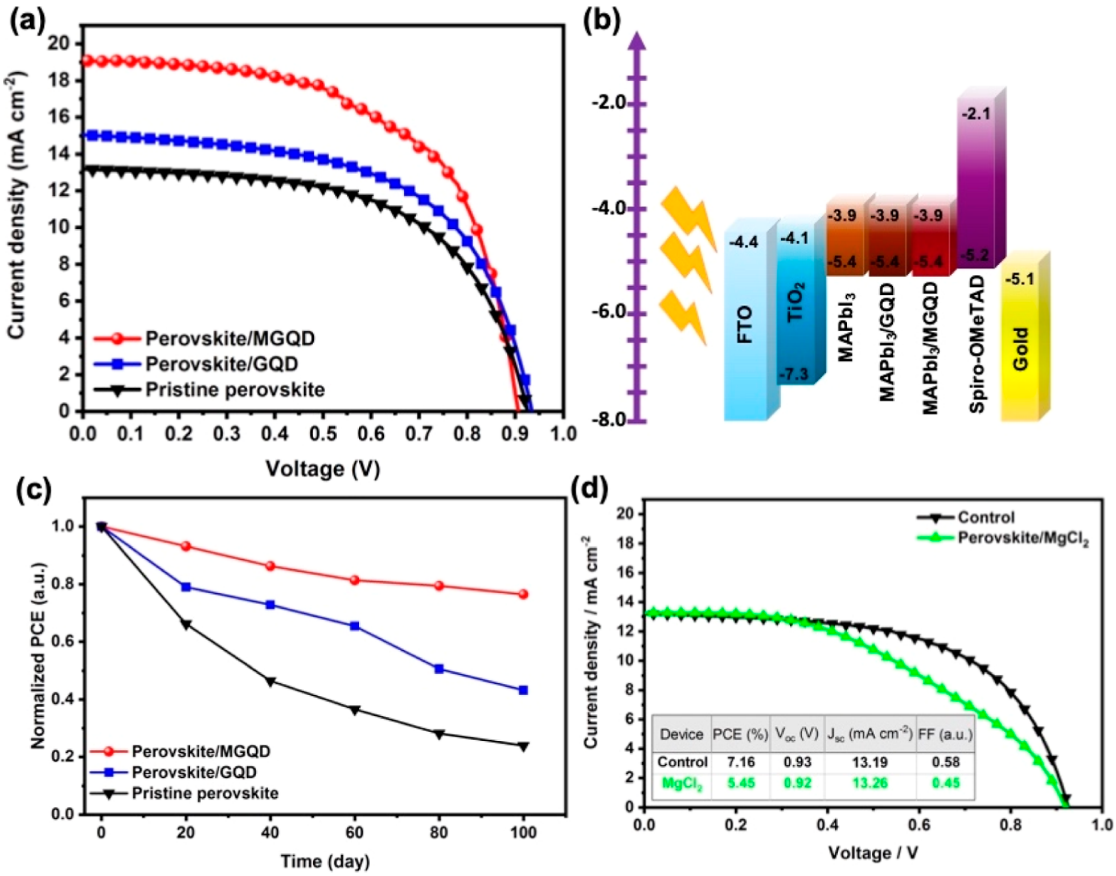

Figure 8. (a) Record $J-V$ curves, (b) energy band diagram, (c) long-term device stability including normalized PCE of pristine perovskite (black), perovskite/GQD (blue), and perovskite/MGQD (red) of fabricated solar devices under the ambient condition (35−40% RH) at room temperature and without any encapsulation, over 100 days, and (d) $J-V$ curve of fabricated devices based on the $MgCl_2$ treatment of perovskite (green) compared to the pristine perovskite (black). The inset table shows the related PV parameters.

PL emission peak of perovskite/MGQD is blue-shifted compared to that of perovskite/GQD. This observation could be due to the interaction of Mg^{2+} with the π-electron of GQD, which results in a blue shift of perovskite/MGQD. The time-resolved PL (TRPL) and decay transients of pristine perovskite and perovskite-modified samples with GQD and MGQD deposited on glass substrates were conducted as shown in Figure 7c. The obtained curves are fitted by a double-exponential decay model, resulting in two components (τ_1 and τ_2). The short-lived τ_1 stands for the monomolecular recombination time, while the long-lived τ_2 reflects the time for the recombination of charges. Table 1 summarizes the fitting parameters from the fitted TRPL curves. The average decay time (τ_{avg}) of the pristine perovskite sample is found to be 3 ns, while the GQD- and MGQD-doped perovskites have 12 and 40 ns lifetimes, respectively. It shows a remarkably longer carrier lifetime (40 ns) for MGQD-doped perovskite in comparison with the pristine perovskite sample (3 ns), which indicates an outstandingly reduced recombination rate in the perovskite film. Thus, the MGQD-doped perovskite film significantly retards the recombination time of the generated electrons and holes and increases the charge carrier lifetime, which means that trap states have been passivated effectively and result in efficient charge extraction to ETL and HTL.[71] It is worth mentioning that the TRPL curve of pristine perovskite revealed a multiexponential behavior instead of a clear biexponential decay (as can be seen in GQD- and MGQD-doped samples), which is considered to be due to the nonradiative recombination at the perovskite bulk and surface or the additional radiative recombination caused by the high excited carrier density.[72]

2.3. Photovoltaic Device Performance. Finally, three types of solar devices based on FTO/TiO_2/perovskite (pristine perovskite, perovskite/GQD, and perovskite/MGQD)/spiro-OMeTAD/Au layers were assembled, and their current density (J)−voltage (V) specifications were evaluated under the same

https://doi.org/10.1021/acsomega.3c04734
ACS Omega 2023, 8, 38345−38358

Table 2. Photovoltaic Device Parameters (V_{OC}, J_{SC}, FF, and PCE) for Pristine Perovskite-, Perovskite/GQD-, and Perovskite/MGQD-Fabricated Solar Devices

device		PCE (%)	V_{OC} (V)	J_{SC} (mA cm^{-2})	FF (a.u.)
pristine perovskite	record	7.16	0.93	13.19	0.58
	average	5.4 ± 1.32	0.89 ± 0.02	11.26 ± 2.48	0.54 ± 0.03
perovskite/GQD	record	8.17	0.94	15.04	0.58
	average	6.45 ± 0.95	0.89 ± 0.02	11.93 ± 1.47	0.56 ± 0.02
perovskite/MGQD	record	10.23	0.9	19.07	0.60
	average	7.39 ± 1.37	0.87 ± 0.03	14.87 ± 2.29	0.57 ± 0.03

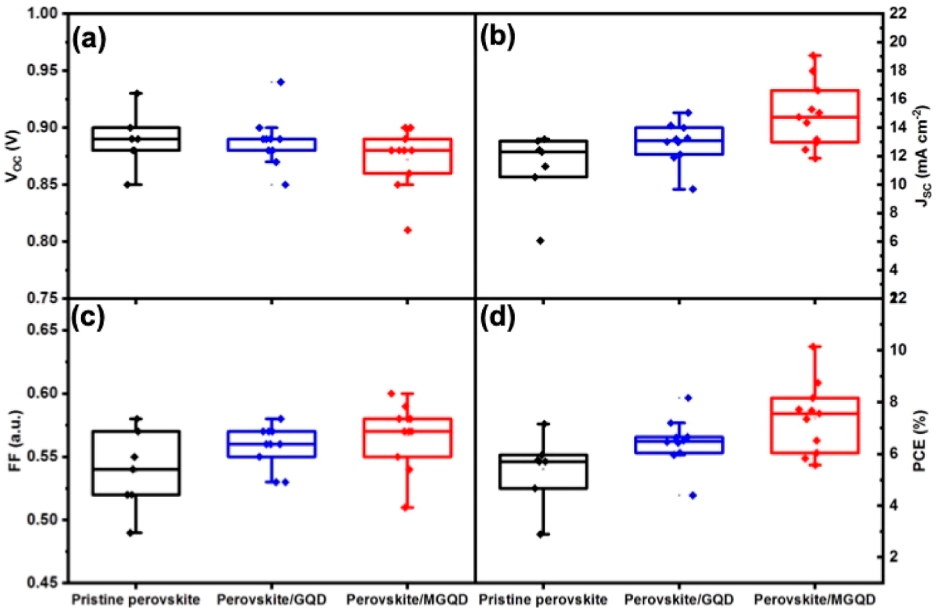

Figure 9. Statistical photovoltaic parameters (a) V_{OC}, (b) J_{SC}, (c) FF, and (d) PCE for pristine perovskite (black), perovskite/GQD (blue), and perovskite/MGQD (red) fabricated solar devices.

conditions to investigate the effect of the MGQD additive on the performance of typical PSCs. Figure 8a shows the recorded $J-V$ curves of the fabricated devices based on untreated (pristine perovskite) and treated perovskite layers containing GQD (perovskite/GQD) and MGQD (perovskite/MGQD), and the related device performance is shown in Table 2. The band energy diagram of the fabricated devices is shown in Figure 8b, where efficient charge carrier extraction and light harvesting lead to the distinct performance of the PV devices. Moreover, Figure 8c indicates the stability of the PSCs based on pristine perovskite and treated perovskite layers containing GQD (perovskite/GQD) and MGQD (perovskite/MGQD), which were monitored over a 100 day period in the ambient condition with a relative humidity (RH) of 35−40% at room temperature without any encapsulation. According to these results, the fabricated devices based on perovskite/GQD and perovskite/MGQD showed improved stability compared with the untreated devices. The perovskite/GQD and perovskite/MGQD-based devices retained 50 and 80% of their initial PCEs after 100 days, respectively. However, the devices based on pristine perovskites undergo rapid degradation (20% of initial PCEs). The substantially improved stability of the perovskite/MGQD-containing devices is attributed to protected grain boundaries with lower recombination centers and a more hydrophobic surface of the modified film.

As a comparison, we fabricated devices with only $MgCl_2$ as a dopant to the perovskite layer to verify the beneficial effect of MGQD on the performance of PSCs. As can be seen in Figure 8d, $MgCl_2$ treatment resulted in a decrease in PV performance compared to the control devices with a pristine perovskite layer, where the PCE decreased from 7.16 to 5.45%. As can be seen in the inset table of Figure 8d, the main reason for the low performance of $MgCl_2$ treatment devices resulted from the diminished fill factor (FF), which is attributed to the increased recombination center in the presence of Mg^{2+} ions.

The statistics of PV indicators, including short-circuit current density (J_{sc}), open-circuit voltage (V_{oc}), FF, and PCE, are shown in Figure 9a−d. Every box in Figure 9 depicts the PV parameter distribution of at least seven devices under the same operating condition.

The beneficial role of MGQDs compared to GQD was verified by the $J-V$ curves. Accordingly, the average PCE, J_{SC}, and FF increased when the GQDs and MGQDs were incorporated into the perovskite layer. The PSCs with perovskite/GQD and perovskite/MGQD layers achieved record PCEs of 8.17 and 10.23%, respectively, whereas the control PSCs achieved a lower PCE of 7.16%.

It is worth mentioning that the modest performance of the control devices (7.16%) was mainly attributed to the purity of the precursors and the anhydrous nature of the solvents, where even homemade precursors such as methylamine iodide (MAI) were used. In addition, day-changing ambient air environmental conditions (as mentioned in the Experimental Section) affect the crystal growth and morphology of the layers compared to the inert, stable, and reproducible atmosphere of the N_2-filled glovebox.

https://doi.org/10.1021/acsomega.3c04734
ACS Omega 2023, 8, 38345−38358

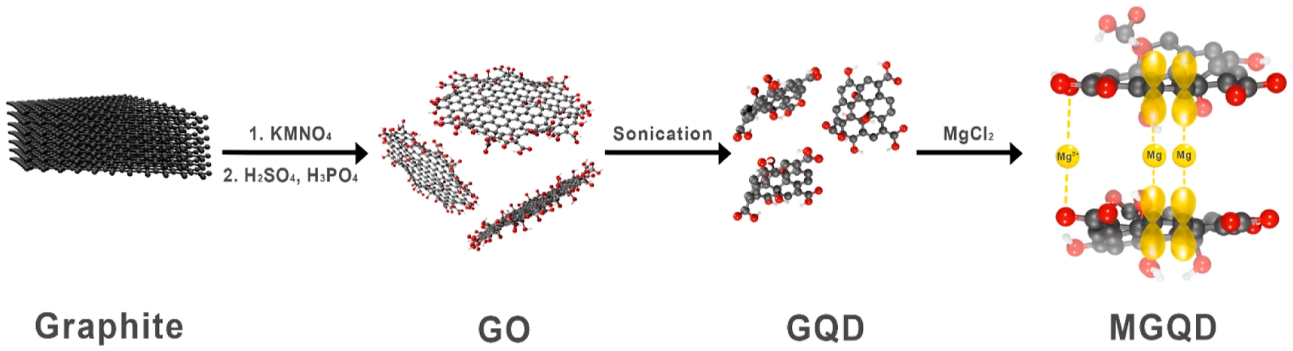

Figure 10. Graphic illustration of the synthesis steps of the magnesium-decorated graphene-quantum dot (MGQD).

Therefore, the highest PCE has been attributed to perovskite/MGQD-based fabricated devices. Moreover, the J_{sc} had a significant enhancement from 13.19 to 19.07 mA cm^{-2} when MGQD was incorporated in the perovskite layer, which implied a higher absorption coefficient (UV−vis spectrum, Figure 7a), better crystallinity of the perovskite crystals (XRD pattern, Figure 6a−c), and larger grain sizes (see FE-SEM images, Figure 5e,f).

Moreover, the average FF was increased for all of the perovskite/MGQD devices, which implied efficient synergistic trap passivation. An approximately 40% increase in PCE for the perovskite/MGQD sample compared with pristine perovskite was mainly implied by the larger grain size when MGQD was added to the perovskite layer. Therefore, the grain boundaries and the pinhole density in the perovskite film decreased drastically, which caused better charge transfer and reduced recombination (Figure 7b). The increase in J_{sc} was also attributed to an increment in the absorption of perovskite/MGQD compared to pristine perovskite (Figure 7a), leading to more capability of the perovskite/MGQD sample in converting light to electricity. The increased value of the FF factor was due to less charge recombination in the TiO_2/perovskite interface caused by a decrease in the number of pinhole defects in the perovskite/MGQD sample. It can be concluded that the MGQD played remarkable multifunctional roles: (i) it retarded the crystallization process, since during the annealing process, the color of the perovskite layer turned dark much slower than the pristine perovskite layer, and this caused the perovskite crystal to grow larger, (ii) it facilitated eased charge extraction, and (iii) it decreased the pinhole density of defects and suppressed the charge recombination rate.

3. CONCLUSIONS

The GQD was successfully synthesized from GO using an ultrasonic-assisted method, and subsequently, it was decorated with $MgCl_2$ (MGQD). The possible mechanism of decorating Mg^{2+} into the GQD structure was through the interaction of Mg^{2+} with oxygen-containing groups or π electrons of C=C bonds. Based on the results, introducing Mg^{2+} to GQD caused a blue shift in $n \rightarrow \pi^*$ and a red shift in $\pi \rightarrow \pi^*$ absorbance peak of GQD, indicating the effective interaction between Mg^{2+} and the functional groups of GQD. The results also demonstrated that decorating Mg^{2+} ions in the GQD structure caused an increase in the crystal size of GQD. The characterized GQDs and MGQDs were dispersed in a perovskite precursor solution, and their effects on the properties of the perovskite layer were studied extensively. The FE-SEM images and XRD analysis showed that MGQD with a larger crystal size compared to GQD could effectively retard the crystallization process, enhance the perovskite grain size, and hence decrease the grain boundaries and pinhole defects in the perovskite layer. In addition, the implementation of MGQD into the perovskite layer assisted in maximizing the light absorption and also decreased the PL intensity of the perovskite layer because of the luminescence-quenching phenomenon and enhanced charge carrier extraction and lifetime (from 3 to 40 ns). Finally, the applicability of GQD and MGQD in PSCs was investigated by incorporating them into a perovskite layer. The perovskite/MGQD indicated the greatest enhancement in the PV parameters of PSCs with an increment of PCE from 7.16 to 10.23%. Consequently, the introduction of MGQD into the perovskite layer was an efficient strategy for better charge extraction as well as the suppression of pinholes and charge recombination in PSCs.

4. EXPERIMENTAL SECTION

4.1. Materials. Graphite powder (size <150 μm, 99.99%), potassium permanganate ($KMnO_4$, > 99%), magnesium chloride ($MgCl_2$, 99.9%), lead(II) iodide (PbI_2, 99.999%), lead(II) bromide ($PbBr_2$, 99.999%), 4-*tert*-butylpyridine, and lithium bis(trifluoromethanesulfonyl) imide (Li-TFSI, 99.8%) were obtained from Sigma-Aldrich Co. Hydrogen peroxide (H_2O_2, 30 wt %), sulfuric acid (H_2SO_4), hydrochloric acid (HCl), phosphoric acid (H_3PO_4), titanium tetrachloride ($TiCl_4$), TiO_2 (composed of 25 nm nanoparticles), titanium isopropoxide (TTIP), and acetone were purchased from Merck Co. Acetonitrile, *N*,*N*-dimethylformamide (DMF), diethyl ether, and chlorobenzene were obtained from Alfar Aesar Chemical Reagent Co. MA bromide (MABr) and formamidinium iodide were purchased from Shanghai Materwin New Materials Co., Ltd. 2,2′,7,7′-tetrakis (*N*,*N*-di-*p*-methoxyphenylamine)-9,9-spirobifluorene (Spiro-OMeTAD) was supplied from Luminescence Technology Co. For solution processing, Milli-Q water (18.2 MΩ cm, Millipore) was used. Laser-patterned FTO with a thickness of 2.2 mm and a sheet resistance of 15 Ω/Sq was purchased from Pilkington.

4.2. Synthesis of Magnesium-Decorated GQDs. First, GO was prepared from graphite powder adopting Ranjan's method.[73] Briefly, graphite powder and $KMnO_4$ with a weight ratio of 1:6 were crushed and dry-ground manually in a porcelain mortar for 5 min and stored at 5 °C. Then, a blend of H_2SO_4/H_3PO_4 (volume ratio of 9:1) held at 5 °C was gently added to the above-prepared mixture while continually stirring at room temperature, resulting in a greenish-black solution. The temperature of the solution was then increased to 65 °C

https://doi.org/10.1021/acsomega.3c04734
ACS Omega 2023, 8, 38345−38358

and kept under stirring and reflux conditions for 24 h. By the end of the reaction, a brownish solution was obtained. After cooling to room temperature, the solution was moved to a beaker that had 400 mL of DI water-ice cubes, and 7 mL of H_2O_2 was added dropwise during magnetic stirring. The golden yellow color of the solution indicates the formation of GO. In the next step, distilled water was added to the produced mixture to complete the precipitation process. The mixture was centrifuged at 10,000 rpm for 5 min, and the supernatant fluid was discarded; the remaining sedimentation was washed with deionized water, HCl, and ethanol, respectively, followed by degasification in a vacuum oven.

In the next step, the obtained GO powder was dispersed in 4 mL of DI water and sonicated in an ultrasonic bath at 40 kHz. After 4 h of sonication, a gray solution along with a residual precipitate was obtained. The supernatant liquid, which is a dispersion of GQD in water, was separated from the sediment by centrifugation at 10,000 rpm for 30 min and dried in an oven at 70 °C for 24 h. The color of the aqueous solution was gray, and the production yield was about 3%.

Finally, 0.2 g of GQD powder was dispersed in 100 mL of DI water and sonicated for 1 h to obtain a uniformly dispersed GQD solution. Then, 0.04 g of $MgCl_2{\cdot}6H_2O$ was dissolved in 7 mL of deionized water and added to the GQD solution. The above-mixed solution was charged into a 60 mL Teflon-lined autoclave and heated at 190 °C for 6 h. After the reaction was completed, the obtained solution was dried in an oven at 60 °C to yield magnesium-decorated GQD (MGQD). The synthesis steps of MGQD are schematically depicted in Figure 10.

4.3. Fabrication of the PSC Device. *4.3.1. Substrate Preparation and $TiCl_4$ Treatment.* Laser-patterned FTO glass was cleaned sequentially in 2% Hellmanex cleaning solution, DI water, HCl/ethanol solution, acetone, and ethanol under 15 min of sonication, followed by drying in nitrogen gas. Then, the clean substrates were exposed to UV−ozone for 15 min and finally dried at 500 °C to remove any organic pollutants. To obtain a TiO_2 solution, HCl/ethanol solution (27.2 mM) was added dropwise to an ethanol solution containing 0.43 M TTIP under vigorous stirring, followed by filtering of the obtained solution via a 0.45 μm polytetrafluoroethylene polymer syringe filter. A 50 nm thick compact layer of TiO_2 as a hole-blocking layer (FTO/bl-TiO_2) was applied on FTO by dynamic spin-coating of TiO_2 solution at 2000 rpm for 30 s, followed by sintering at 500 °C for 30 min. Meso-porous TiO_2 layer (particle size of 20−25 nm and anatase crystalline phase) was obtained by spin-coating SHARIFSOLAR transparent TiO_2 pastes diluted in ethanol (1:2 weight ratio) at 2000 rpm. for 30 s on the FTO/bl-TiO_2 substrate. The resulting film was exposed to ethanol vapor and annealed at 120 °C for 6 min, and the sintering procedure was conducted at 500 °C for 30 min under airflow. To further boost the electrical conductivity of the meso-porous TiO_2 layer, the substrates were soaked in the $TiCl_4$ aqueous solution (0.04 M) at 70 °C for 30 min, where the residual species were washed with DI water and ethanol, following drying at 500 °C for 30 min.

4.3.2. Perovskite Precursor Solution and Layer Preparation. A $MAPbI_3$ precursor solution (40 wt %) was prepared as described elsewhere.[74] Briefly, MAI was prepared by adding 30 mL of aqueous solution of hydroiodic acid (57 wt %) to 270.8 mL of methylamine solution (40 wt % in methanol) placed in an ice bath and stirring for 2 h. Then, the solution was kept at 50 °C for 1 h to be evaporated, which was washed several times with diethyl ether, dissolved again in ethanol, and air-dried for 24 h. Then, the readily synthesized MAI (0.253 g) and commercially available PbI_2 (0.147 g) with a molar ratio of 3:1 were mixed in DMF and magnetically stirred at 70 °C for 30 min. The obtained $MAPbI_3$ precursor solution was kept at 70 °C in a dark place overnight. To prepare the GQD or MGQD-decorated $MAPbI_3$ solution, GQD or MGQDs (0.001 g) were added to the prepared $MAPbI_3$ precursor solution (10 mL) and stirred for 30 min. Finally, pristine perovskite, perovskite/GQD, and perovskite/MGQD layers were deposited by spin-coating of the $MAPbI_3$-, GQD-, and MGQD-decorated $MAPbI_3$ precursor solution on the mesoporous TiO_2-coated substrate at 2500 rpm for 45 s, respectively, and dried at 90 °C for 15 min. It is worth mentioning that all the solution and deposition processes of the device fabrication were performed in the ambient atmosphere, with a RH of 35−40%.

4.3.3. Hole Transporting Material and Back Electrode. A hole-transport material solution from 72.3 mg of spiro-OMeTAD, 28.8 μL of 4-*tert*-butylpyridine, and 17.5 μL of lithium bis (trifluoromethanesulfonyl) imide (Li-TFSI) solution (520 mg of Li-TSFI dissolved in 1 mL of acetonitrile) in 1 mL of chlorobenzene was spin coated on the top of the perovskite layer at 4000 rpm. for 30 s. At the last step, an 80-thick gold electrode was deposited on the spiro-OMeTAD-coated film under 10^{-7} mbar high vacuum pressure.

4.4. Characterization Methods. FTIR spectra of GO, GQD, and MGQD were acquired using an FT-IR BRUKER-IFS48 spectrophotometer (Germany) with 16 scans at a resolution of 4 cm^{-1} and a range of 400−4000 cm^{-1}. The chemical states of the MGQD were examined using XPS (Thermo Fisher Scientific K-Alpha, USA). Moreover, the optical properties (UV−vis analysis) of the GO, GQD, MGQD, and perovskite films were taken by a spectrophotometer (PerkinElmer Lambda 365 UV−vis, USA). To investigate the crystal structure of samples, XRD was done with an XPERT-PRO diffractometer using Cu Kα radiation (λ = 1.54059 Å, 40 kV, 40 mA) at a scanning rate of 1.2 min^{-1} in the 2θ range. High-resolution transmission electron microscopy images of GQD and MGQD were acquired on a Philips EM208S (Royal Dutch Philips Electronics Ltd., Eindhoven, Netherlands), which is operated at 100 kV. To calculate the diameter of particles in different TEM micrographs, image processing software (ImageJ, version 1.51) was employed. The AFM (VEECO-CP research) analysis was conducted to investigate the top surface topology of the perovskite films with a silicon tip of 10 nm radius in noncontact mode. The top surface morphology and grain sizes of the perovskite layer were characterized utilizing a FE-SEM (MIRA3, TESCAN, Czech Republic) by accelerating the operation voltage of 15 kV. To get a better image resolution from the semiconducting perovskite films, a thin layer of gold was coated under an inert argon atmosphere using an Emitech K450x sputter-coating system (England). The PL spectrum of the perovskite films was measured with a spectrophotometer (Avaspec 2048-TEC) by using an integrating sphere, where a pulsed laser (405 nm wavelength and 1 MHz frequency) was employed to excite the samples. The TRPL test of perovskite-deposited film with and without GQD and MGQD was measured by an FLS980 fluorescence spectrometer from Edinburgh Instruments. TRPL is performed at an excitation wavelength of 520 nm and responds to the entire emission spectrum. All optical measurements were carried out at room temperature. The current density−voltage (J−V) characteristics were measured

https://doi.org/10.1021/acsomega.3c04734
ACS Omega 2023, 8, 38345−38358

by a PalmSense 2400 source meter (scan rate of 50 mV s^{-1}) under light using a solar simulator (Sharif solar, SIM-1000, AM 1.5 G light, 100 mW cm^{-2}) calibrated with a silicon photodiode (Thorlabs). The active area of all pixels was defended with an optical mask with an aperture of 0.09 cm^2.

■ ASSOCIATED CONTENT

Supporting Information

The Supporting Information is available free of charge at https://pubs.acs.org/doi/10.1021/acsomega.3c04734.

TEM images and size distribution histograms of GQD and MGQD samples (PDF)

■ AUTHOR INFORMATION

Corresponding Author

Fatemeh Rahnemaye Rahsepar − *School of Chemistry, College of Science, University of Tehran, Tehran 1417614411, Iran;* orcid.org/0000-0003-2359-2523; Email: frahsepar@ut.ac.ir

Authors

Somayeh Kalanaki − *Chemistry Department, Kish International Campus, University of Tehran, Tehran 1417633644, Iran*

Yaser Abdi − *Nanophysics Lab., Department of Physics, University of Tehran, Tehran 141761441, Iran;* orcid.org/0000-0002-7583-7687

Complete contact information is available at: https://pubs.acs.org/10.1021/acsomega.3c04734

Author Contributions

The manuscript was written through the contributions of all authors. All authors have given approval to the final version of the manuscript.

Funding

This research did not receive any specific grants from funding agencies in the public, commercial, or not-for-profit sectors.

Notes

The authors declare no competing financial interest.

■ REFERENCES

(1) Kumari, T. S. D. Catalytic Graphitization: A Bottom-up Approach to Graphene and Quantum Dots Derived Therefrom - A Review. *Mater. Today: Proc.* **2021**, *46*, 3069−3074.

(2) Kang, H.; Kim, D. Y.; Cho, J. Top-Down Fabrication of Luminescent Graphene Quantum Dots Using Self-Assembled Au Nanoparticles. *ACS Omega* **2023**, *8* (6), 5885−5892.

(3) Kanwal, S.; Jahan, S.; Mansoor, F. An Ultrasonic-Assisted Synthesis of Leather-Derived Luminescent Graphene Quantum Dots: Catalytic Reduction and Switch on-off Probe for Nitro-Explosives. *RSC Adv.* **2020**, *10* (39), 22959−22965.

(4) Yan, Y.; Manickam, S.; Lester, E.; Wu, T.; Pang, C. H. Synthesis of Graphene Oxide and Graphene Quantum Dots from Miscanthus via Ultrasound-Assisted Mechano-Chemical Cracking Method. *Ultrason. Sonochem.* **2021**, *73*, 105519.

(5) Chen, W.; Lv, G.; Hu, W.; Li, D.; Chen, S.; Dai, Z. Synthesis and Applications of Graphene Quantum Dots: A Review. *Nanotechnol. Rev.* **2018**, *7* (2), 157−185.

(6) Xia, B.; Tu, M.; Pradhan, B.; Ceyssens, F.; Tietze, M. L.; Rubio-Giménez, V.; Wauteraerts, N.; Gao, Y.; Kraft, M.; Steele, J. A.; Debroye, E.; Hofkens, J.; Ameloot, R. Flexible Metal Halide Perovskite Photodetector Arrays via Photolithography and Dry Lift-Off Patterning. *Adv. Eng. Mater.* **2022**, *24* (1), 2100930.

(7) Pintor Monroy, M. I.; Goldberg, I.; Elkhouly, K.; Georgitzikis, E.; Clinckemalie, L.; Croes, G.; Annavarapu, N.; Qiu, W.; Debroye, E.; Kuang, Y.; Roeffaers, M. B. J.; Hofkens, J.; Gehlhaar, R.; Genoe, J. All-Evaporated, All-Inorganic CsPbI3 Perovskite-Based Devices for Broad-Band Photodetector and Solar Cell Applications. *ACS Appl. Electron. Mater.* **2021**, *3* (7), 3023−3033.

(8) Sharma, V.; Jha, P. K. Enhancement in Power Conversion Efficiency of Edge-Functionalized Graphene Quantum Dot through Adatoms for Solar Cell Applications. *Sol. Energy Mater. Sol. Cells* **2019**, *200*, 109908.

(9) Ibn-Mohammed, T.; Koh, S. C. L.; Reaney, I. M.; Acquaye, A.; Schileo, G.; Mustapha, K. B.; Greenough, R. Perovskite Solar Cells: An Integrated Hybrid Lifecycle Assessment and Review in Comparison with Other Photovoltaic Technologies. *Renewable Sustainable Energy Rev.* **2017**, *80*, 1321−1344.

(10) Rahighi, R.; Gholipour, S.; Amin, M. A.; Ansari, M. Z. Hole-Transport Material Engineering in Highly Durable Carbon-Based Perovskite Photovoltaic Devices. *Nanomaterials* **2023**, *13* (8), 1417.

(11) Snaith, H. J. Perovskites: The Emergence of a New Era for Low-Cost, High-Efficiency Solar Cells. *J. Phys. Chem. Lett.* **2013**, *4* (21), 3623−3630.

(12) Graetzel, M.; Janssen, R. A. J.; Mitzi, D. B.; Sargent, E. H. Materials Interface Engineering for Solution-Processed Photovoltaics. *Nature* **2012**, *488* (7411), 304−312.

(13) Shahjahan, M. D.; Okamoto, T.; Chouhan, L.; Sachith, B. M.; Pradhan, N.; Misawa, H.; Biju, V. Halide Perovskite Single Crystals and Nanocrystal Films as Electron Donor-Acceptor Heterojunctions. *Angew. Chem., Int. Ed.* **2023**, *62* (4), No. e202215947.

(14) Sachith, B. M.; Zhang, Z.; Subramanyam, P.; Subrahmanyam, C.; Furube, A.; Tamai, N.; Okamoto, T.; Misawa, H.; Biju, V. Photoinduced Interfacial Electron Transfer from Perovskite Quantum Dots to Molecular Acceptors for Solar Cells. *Nanoscale* **2023**, *15* (17), 7695−7702.

(15) Chouhan, L.; Ghimire, S.; Subrahmanyam, C.; Miyasaka, T.; Biju, V. Synthesis, Optoelectronic Properties and Applications of Halide Perovskites. *Chem. Soc. Rev.* **2020**, *49* (10), 2869−2885.

(16) Zhang, X.; Turiansky, M. E.; Shen, J.-X.; Van de Walle, C. G. Defect Tolerance in Halide Perovskites: A First-Principles Perspective. *J. Appl. Phys.* **2022**, *131* (9), 090901.

(17) Kojima, A.; Teshima, K.; Shirai, Y.; Miyasaka, T. Organometal Halide Perovskites as Visible-Light Sensitizers for Photovoltaic Cells. *J. Am. Chem. Soc.* **2009**, *131* (17), 6050−6051.

(18) Park, J.; Kim, J.; Yun, H.-S.; Paik, M. J.; Noh, E.; Mun, H. J.; Kim, M. G.; Shin, T. J.; Seok, S. I. Controlled Growth of Perovskite Layers with Volatile Alkylammonium Chlorides. *Nature* **2023**, *616*, 724−730.

(19) Best Research-Cell Efficiency Chart, Photovoltaic Research; NREL: Golden, CO, USA, 2023. https://www.nrel.gov/pv/cell-efficiency.html (accessed May 19, 2023).

(20) Yu, Y.; Xia, J.; Liang, Y. Basic Understanding of Perovskite Solar Cells and Passivation Mechanism. *AIP Adv.* **2022**, *12* (5), 055307.

(21) Hatamvand, M.; Gholipour, S.; Chen, M.; Zhou, Y.; Jiang, T.; Hu, Z.; Chen, Y.; Huang, W. Dual-Side Interfacial Passivation of FAPbI3 Perovskite Film by Naphthylmethylammonium Iodide for Highly Efficient and Stable Perovskite Solar Cells. *Chem. Eng. J.* **2023**, *460*, 141788.

(22) Shadrokh, Z.; Sousani, S.; Gholipour, S.; Abdi, Y. Enhanced Stability and Performance of Poly(4-Vinylpyridine) Modified Perovskite Solar Cell with Quaternary Semiconductor Cu2MSnS4 (M= Co2+, Ni2+, Zn2+) as Hole Transport Materials. *Sol. Energy Mater. Sol. Cells* **2020**, *211*, 110538.

(23) Shadrokh, Z.; Sousani, Sh.; Gholipour, S.; Abdi, Y. Enhanced Photovoltaic Performance and Stability of Perovskite Solar Cells by Interface Engineering with Poly(4-Vinylpyridine) and Cu2ZnSnS4&CNT. *Sol. Energy* **2020**, *201*, 908−915.

(24) Tai, Q.; Tang, K.-C.; Yan, F. Recent Progress of Inorganic Perovskite Solar Cells. *Energy Environ. Sci.* **2019**, *12* (8), 2375−2405.

(25) Jena, A. K.; Gholipour, S.; Abdi, Y.; Saliba, M. Perovskite Photovoltaics. In *Springer Handbook of Inorganic Photochemistry*; Bahnemann, D., Patrocinio, A. O. T., Eds.; *Springer Handbooks*; Springer International Publishing: Cham, 2022; pp 1267−1303.
(26) Lu, C.; Zhang, W.; Jiang, Z.; Zhang, Y.; Ni, C. Graphene Quantum Dots Doping SnO2 for Improving Carrier Transport of Perovskite Solar Cells. *Ceram. Int.* **2021**, *47* (21), 29712−29721.
(27) Pham, N. D.; Tiong, V. T.; Chen, P.; Wang, L.; Wilson, G. J.; Bell, J.; Wang, H. Enhanced Perovskite Electronic Properties via a Modified Lead(II) Chloride Lewis Acid-Base Adduct and Their Effect in High-Efficiency Perovskite Solar Cells. *J. Mater. Chem. A* **2017**, *5* (10), 5195−5203.
(28) Kim, T.; Lim, J.; Song, S. Recent Progress and Challenges of Electron Transport Layers in Organic-Inorganic Perovskite Solar Cells. *Energies* **2020**, *13* (21), 5572.
(29) Yun, J.; Jun, J.; Yu, H.; Lee, K.; Ryu, J.; Lee, J.; Jang, J. Highly Efficient Perovskite Solar Cells Incorporating NiO Nanotubes: Increased Grain Size and Enhanced Charge Extraction. *J. Mater. Chem. A* **2017**, *5* (41), 21750−21756.
(30) Byranvand, M. M.; Song, S.; Pyeon, L.; Kang, G.; Lee, G.-Y.; Park, T. Simple Post Annealing-Free Method for Fabricating Uniform, Large Grain-Sized, and Highly Crystalline Perovskite Films. *Nano Energy* **2017**, *34*, 181−187.
(31) Wang, P.; Zhang, X.; Zhou, Y.; Jiang, Q.; Ye, Q.; Chu, Z.; Li, X.; Yang, X.; Yin, Z.; You, J. Solvent-Controlled Growth of Inorganic Perovskite Films in Dry Environment for Efficient and Stable Solar Cells. *Nat. Commun.* **2018**, *9* (1), 2225.
(32) Hadadian, M.; Correa-Baena, J.-P.; Goharshadi, E. K.; Ummadisingu, A.; Seo, J.-Y.; Luo, J.; Gholipour, S.; Zakeeruddin, S. M.; Saliba, M.; Abate, A.; Grätzel, M.; Hagfeldt, A. Enhancing Efficiency of Perovskite Solar Cells via N-Doped Graphene: Crystal Modification and Surface Passivation. *Adv. Mater.* **2016**, *28* (39), 8681−8686.
(33) Chen, H.; Luo, Q.; Liu, T.; Tai, M.; Lin, J.; Murugadoss, V.; Lin, H.; Wang, J.; Guo, Z.; Wang, N. Boosting Multiple Interfaces by Co-Doped Graphene Quantum Dots for High Efficiency and Durability Perovskite Solar Cells. *ACS Appl. Mater. Interfaces* **2020**, *12* (12), 13941−13949.
(34) Pang, S.; Zhang, C.; Zhang, H.; Dong, H.; Chen, D.; Zhu, W.; Xi, H.; Chang, J.; Lin, Z.; Zhang, J.; Hao, Y. Boosting Performance of Perovskite Solar Cells with Graphene Quantum Dots Decorated SnO2 Electron Transport Layers. *Appl. Surf. Sci.* **2020**, *507*, 145099.
(35) Zhang, J.; Tong, T.; Zhang, L.; Li, X.; Zou, H.; Yu, J. Enhanced Performance of Planar Perovskite Solar Cell by Graphene Quantum Dot Modification. *ACS Sustainable Chem. Eng.* **2018**, *6*, 8631−8640.
(36) Fang, X.; Ding, J.; Yuan, N.; Sun, P.; Lv, M.; Ding, G.; Zhu, C. Graphene Quantum Dot Incorporated Perovskite Films: Passivating Grain Boundaries and Facilitating Electron Extraction. *Phys. Chem. Chem. Phys.* **2017**, *19* (8), 6057−6063.
(37) Wang, P.; Jiang, Q.; Zhao, Y.; Chen, Y.; Chu, Z.; Zhang, X.; Zhou, Y.; You, J. Synergistic Improvement of Perovskite Film Quality for Efficient Solar Cells via Multiple Chloride Salt Additives. *Sci. Bull.* **2018**, *63* (11), 726−731.
(38) Rong, Y.; Hou, X.; Hu, Y.; Mei, A.; Liu, L.; Wang, P.; Han, H. Synergy of Ammonium Chloride and Moisture on Perovskite Crystallization for Efficient Printable Mesoscopic Solar Cells. *Nat. Commun.* **2017**, *8* (1), 14555.
(39) Yavari, M.; Mazloum-Ardakani, M.; Gholipour, S.; Tavakoli, M. M.; Taghavinia, N.; Hagfeldt, A.; Tress, W. Reducing Surface Recombination by a Poly(4-Vinylpyridine) Interlayer in Perovskite Solar Cells with High Open-Circuit Voltage and Efficiency. *ACS Omega* **2018**, *3* (5), 5038−5043.
(40) Zhang, X.; Qiu, W.; Song, W.; Hawash, Z.; Wang, Y.; Pradhan, B.; Zhang, Y.; Naumenko, D.; Amenitsch, H.; Moons, E.; Merckx, T.; Aguirre, A.; Abdulraheem, Y.; Aernouts, T.; Zhan, Y.; Kuang, Y.; Hofkens, J.; Poortmans, J. An Integrated Bulk and Surface Modification Strategy for Gas-Quenched Inverted Perovskite Solar Cells with Efficiencies Exceeding 22%. *Sol. RRL* **2022**, *6* (6), 2200053.
(41) Hadadian, M.; Smått, J.-H.; Correa-Baena, J.-P. The Role of Carbon-Based Materials in Enhancing the Stability of Perovskite Solar Cells. *Energy Environ. Sci.* **2020**, *13* (5), 1377−1407.
(42) Shen, D.; Zhang, W.; Xie, F.; Li, Y.; Abate, A.; Wei, M. Graphene Quantum Dots Decorated TiO2Mesoporous Film as an Efficient Electron Transport Layer for High-Performance Perovskite Solar Cells. *J. Power Sources* **2018**, *402*, 320−326.
(43) Jena, A. K.; Kulkarni, A.; Miyasaka, T. Halide Perovskite Photovoltaics: Background, Status, and Future Prospects. *Chem. Rev.* **2019**, *119* (5), 3036−3103.
(44) Chang, J.; Lin, Z.; Zhu, H.; Isikgor, F. H.; Xu, Q.-H.; Zhang, C.; Hao, Y.; Ouyang, J. Enhancing the Photovoltaic Performance of Planar Heterojunction Perovskite Solar Cells by Doping the Perovskite Layer with Alkali Metal Ions. *J. Mater. Chem. A* **2016**, *4* (42), 16546−16552.
(45) Arshad, Z.; Khoja, A. H.; Shakir, S.; Afzal, A.; Mujtaba, M. A.; Soudagar, M. E. M.; Fayaz, H.; Saleel C, A.; Farukh, S.; Saeed, M. Magnesium Doped TiO2 as an Efficient Electron Transport Layer in Perovskite Solar Cells. *Case Stud. Therm. Eng.* **2021**, *26*, 101101.
(46) Baktash, A.; Amiri, O.; Sasani, A. Improve Efficiency of Perovskite Solar Cells by Using Magnesium Doped ZnO and TiO2 Compact Layers. *Superlattices Microstruct.* **2016**, *93*, 128−137.
(47) Zhang, H.; Shi, J.; Xu, X.; Zhu, L.; Luo, Y.; Li, D.; Meng, Q. Mg-Doped TiO2 Boosts the Efficiency of Planar Perovskite Solar Cells to Exceed 19%. *J. Mater. Chem. A* **2016**, *4* (40), 15383−15389.
(48) Peng, W.; Li, S.; Li, M.; Chen, M.; Yang, Y. Enhancement of the Electron Transportation in the Perovskite Solar Cells via Optimizing the Photoelectric Properties of Electron Transport Layer with Nitrogen-Doped Graphene Quantum Dots. *J. Mater. Sci.: Mater. Electron.* **2022**, *33* (18), 14443−14456.
(49) Le, H. C.; Pham, N. T.; Vu, D. C.; Pham, D. L.; Nguyen, S. H.; Nguyen, T. T. O.; Nguyen, C. D. Nitrogen-Doped Graphene Quantum Dot-Tin Dioxide Nanocomposite Ultrathin Films as Efficient Electron Transport Layers for Planar Perovskite Solar Cells. *Crystals* **2023**, *13* (6), 961.
(50) Bian, H.; Wang, Q.; Yang, S.; Yan, C.; Wang, H.; Liang, L.; Jin, Z.; Wang, G.; Liu, S. F. Nitrogen-Doped Graphene Quantum Dots for 80% Photoluminescence Quantum Yield for Inorganic γ-CsPbI3 Perovskite Solar Cells with Efficiency beyond 16%. *J. Mater. Chem. A* **2019**, *7* (10), 5740−5747.
(51) Gan, X.; Yang, S.; Zhang, J.; Wang, G.; He, P.; Sun, H.; Yuan, H.; Yu, L.; Ding, G.; Zhu, Y. Graphite-N Doped Graphene Quantum Dots as Semiconductor Additive in Perovskite Solar Cells. *ACS Appl. Mater. Interfaces* **2019**, *11* (41), 37796−37803.
(52) Griffin, I. J. Magnesium. *Encyclopedia of Food Sciences and Nutrition*, 2nd ed.; Caballero, B., Ed.; Academic Press: Oxford, 2003; pp 3641−3646.
(53) Lin, X.; Shen, X.; Sun, X.; Liu, X.; Wu, Y.; Wang, Z.; Kim, J.-K. Graphene Oxide Papers Simultaneously Doped with Mg2+ and Cl- for Exceptional Mechanical, Electrical, and Dielectric Properties. *ACS Appl. Mater. Interfaces* **2016**, *8* (3), 2360−2371.
(54) Guerrero-Contreras, J.; Caballero-Briones, F. Graphene Oxide Powders with Different Oxidation Degree, Prepared by Synthesis Variations of the Hummers Method. *Mater. Chem. Phys.* **2015**, *153*, 209−220.
(55) Chhabra, V. A.; Kaur, R.; Kumar, N.; Deep, A.; Rajesh, C.; Kim, K.-H. Synthesis and Spectroscopic Studies of Functionalized Graphene Quantum Dots with Diverse Fluorescence Characteristics. *RSC Adv.* **2018**, *8* (21), 11446−11454.
(56) Wolk, A.; Rosenthal, M.; Neuhaus, S.; Huber, K.; Brassat, K.; Lindner, J. K. N.; Grothe, R.; Grundmeier, G.; Bremser, W.; Wilhelm, R. A Novel Lubricant Based on Covalent Functionalized Graphene Oxide Quantum Dots. *Sci. Rep.* **2018**, *8* (1), 5843.
(57) Moreira, V. R.; Lebron, Y. A. R.; da Silva, M. M.; de Souza Santos, L. V.; Jacob, R. S.; de Vasconcelos, C. K. B.; Viana, M. M. Graphene Oxide in the Remediation of Norfloxacin from Aqueous Matrix: Simultaneous Adsorption and Degradation Process. *Environ. Sci. Pollut. Res.* **2020**, *27* (27), 34513−34528.

https://doi.org/10.1021/acsomega.3c04734
ACS Omega 2023, 8, 38345−38358

(58) Karimi, B.; Ramezanzadeh, B. A Comparative Study on the Effects of Ultrathin Luminescent Graphene Oxide Quantum Dot (GOQD) and Graphene Oxide (GO) Nanosheets on the Interfacial Interactions and Mechanical Properties of an Epoxy Composite. *J. Colloid Interface Sci.* **2017**, *493*, 62−76.
(59) Tang, D.; Liu, J.; Yan, X.; Kang, L. Graphene Oxide Derived Graphene Quantum Dots with Different Photoluminescence Properties and Peroxidase-like Catalytic Activity. *RSC Adv.* **2016**, *6* (56), 50609−50617.
(60) Kumar, S.; Ojha, A. K.; Ahmed, B.; Kumar, A.; Das, J.; Materny, A. Tunable (Violet to Green) Emission by High-Yield Graphene Quantum Dots and Exploiting Its Unique Properties towards Sun-Light-Driven Photocatalysis and Supercapacitor Electrode Materials. *Mater. Today Commun.* **2017**, *11*, 76−86.
(61) Najafi-Shoa, S.; Barikani, M.; Ehsani, M.; Ghaffari, M. Cobalt-Based Ionic Liquid Grafted on Graphene as a Heterogeneous Catalyst for Poly (Ethylene Terephthalate) Glycolysis. *Polym. Degrad. Stab.* **2021**, *192*, 109691.
(62) Porfarzollah, A.; Mohammad-Rezaei, R.; Bagheri, M. Ionic Liquid-Functionalized Graphene Quantum Dots as an Efficient Quasi-Solid-State Electrolyte for Dye-Sensitized Solar Cells. *J. Mater. Sci.: Mater. Electron.* **2020**, *31* (3), 2288−2297.
(63) Durmus, Z.; Kurt, B. Z.; Durmus, A. Synthesis and Characterization of Graphene Oxide/Zinc Oxide (GO/ZnO) Nanocomposite and Its Utilization for Photocatalytic Degradation of Basic Fuchsin Dye. *ChemistrySelect* **2019**, *4* (1), 271−278.
(64) Teymourinia, H.; Salavati-Niasari, M.; Amiri, O.; Farangi, M. Facile Synthesis of Graphene Quantum Dots from Corn Powder and Their Application as down Conversion Effect in Quantum Dot-Dye-Sensitized Solar Cell. *J. Mol. Liq.* **2018**, *251*, 267−272.
(65) Abbas, A.; Rubab, S.; Rehman, A.; Irfan, S.; Sharif, H. M. A.; Liang, Q.; Tabish, T. A. One-Step Green Synthesis of Biomass-Derived Graphene Quantum Dots as a Highly Selective Optical Sensing Probe. *Mater. Today Chem.* **2023**, *30*, 101555.
(66) Kumar, S.; Aziz, S. T.; Girshevitz, O.; Nessim, G. D. One-Step Synthesis of N-Doped Graphene Quantum Dots from Chitosan as a Sole Precursor Using Chemical Vapor Deposition. *J. Phys. Chem. C* **2018**, *122* (4), 2343−2349.
(67) Ahmed, D. S.; Mohammed, M. K. A.; Majeed, S. M. Green Synthesis of Eco-Friendly Graphene Quantum Dots for Highly Efficient Perovskite Solar Cells. *ACS Appl. Energy Mater.* **2020**, *3* (11), 10863−10871.
(68) Awino, C.; Odari, V.; Dittrich, T.; Prajongtat, P.; Sakwa, T.; Rech, B. Investigation of Structural and Electronic Properties of CH3NH3PbI3 Stabilized by Varying Concentrations of Poly(Methyl Methacrylate) (PMMA). *Coatings* **2017**, *7* (8), 115.
(69) Shin, S. H.; Shin, D. H.; Choi, S.-H. Enhancement of Stability of Inverted Flexible Perovskite Solar Cells by Employing Graphene-Quantum-Dots Hole Transport Layer and Graphene Transparent Electrode Codoped with Gold Nanoparticles and Bis-(Trifluoromethanesulfonyl)Amide. *ACS Sustainable Chem. Eng.* **2019**, *7* (15), 13178−13185.
(70) Wu, Z. Y.; Jian, B.-L.; Hsu, H.-C. Photoluminescence Characterizations of Highly Ambient-Air-Stable $CH_3NH_3PbI_3/PbI_2$ Heterostructure. *Opt. Mater. Express* **2019**, *9* (4), 1882−1892.
(71) Jiang, Q.; Zhao, Y.; Zhang, X.; Yang, X.; Chen, Y.; Chu, Z.; Ye, Q.; Li, X.; Yin, Z.; You, J. Surface Passivation of Perovskite Film for Efficient Solar Cells. *Nat. Photonics* **2019**, *13* (7), 460−466.
(72) Li, H.; Di, H.; Wang, X.; Ren, Z.; Lu, M.; Liu, A.-A.; Yang, X.; Wang, N.; Zhao, Y.; Li, B. Diffusion Effect on the Decay of Time-Resolved Photoluminescence under Low Illumination in Lead Halide Perovskites. *Sci. China: Phys., Mech. Astron.* **2023**, *66* (8), 287311.
(73) Ranjan, P.; Agrawal, S.; Sinha, A.; Rao, T. R.; Balakrishnan, J.; Thakur, A. D. A Low-Cost Non-Explosive Synthesis of Graphene Oxide for Scalable Applications. *Sci. Rep.* **2018**, *8* (1), 12007.
(74) Guo, Y.; Shoyama, K.; Sato, W.; Nakamura, E. Polymer Stabilization of Lead(II) Perovskite Cubic Nanocrystals for Semi-transparent Solar Cells. *Adv. Energy Mater.* **2016**, *6* (6), 1502317.

https://doi.org/10.1021/acsomega.3c04734
ACS Omega 2023, 8, 38345−38358